Acta Materialia 232 (2022) 117934

Contents lists available at ScienceDirect

Acta Materialia

journal homepage: www.elsevier.com/locate/actamat

Full length article

Effects of structure relaxation and surface oxidation on nanoscopic wear behaviors of metallic glass

Qian Jia[a,1], Wenhao He[b,1], Dongpeng Hua[a], Qing Zhou[a,*], Yin Du[a], Yue Ren[a], Zhibin Lu[b], Haifeng Wang[a,*], Feng Zhou[b], Jian Wang[c]

[a] State Key Laboratory of Solidification Processing, Center of Advanced Lubrication and Seal Materials, Northwestern Polytechnical University, Xi'an, Shaanxi 710072, PR China
[b] State Key Laboratory of Solid Lubrication, Lanzhou Institute of Chemical Physics, Chinese Academy of Sciences, Lanzhou, 730000, PR China
[c] Mechanical and Materials Engineering, University of Nebraska-Lincoln, Lincoln, NE 68588, USA

ARTICLE INFO

Article history:
Received 23 January 2022
Revised 24 March 2022
Accepted 9 April 2022
Available online 11 April 2022

Keywords:
Metallic glass
Structure relaxation
Oxidation
Nanoscopic wear
Friction mechanism

ABSTRACT

Both structure relaxation and oxidation of surface layer induced by thermal treatment or friction heat play significant roles in reducing wear of metallic glasses (MGs). To distinguish the effects of structure relaxation and surface oxidation, we prepared Zr-based MGs at different states, i.e., as-cast MG; the annealed MGs under argon atmosphere (referred to as structure-relaxed MG) and oxygen atmosphere (referred to as oxidized MG). Nano-wear tests were carried out by atomic force microscope (AFM) to quantitatively clarify these two effects on the wear performance. Compared with the as-cast MG, the structure-relaxed MG shows an increased adhesive but slightly decreased ploughing friction. While, the oxidized MG shows the best anti-wear performance with dramatic reductions in both adhesive and ploughing friction. Classic molecular dynamics (MD) and ab initio MD simulations revealed that the introduction of O hinders the MG atoms from forming interfacial bonds with diamond, and reduces significantly the adhesion between the diamond tip and passivated MG. In addition, the synergistic effect of high hardness and elastic recovery associated with oxidization reduces ploughing friction and enhances wear resistance. This finding clarifies the importance of surface chemistry over structure modification during wear, and offers a generic pathway for tailoring ultra-wear resistant MGs.

© 2022 Acta Materialia Inc. Published by Elsevier Ltd. All rights reserved.

1. Introduction

Metallic glasses (MGs) have attracted a growing interest due to their preeminent properties such as high hardness, large elastic limit, and high tensile strength [1–3]. Previous studies demonstrated that the pre-thermal treatment or friction heat during wear can cause structure relaxation and modify surface chemistry of MGs [4–6]. Structure relaxation is associated with lowering the enthalpy of MGs through annihilating the free volumes and increasing the packing density of MGs, correspondingly, altering the mechanical and tribological performance of MGs [7–9]. Chen et al. [10] confirmed that the $Zr_{50.7}Cu_{28}Ni_9Al_{12.3}$ MG annealed below the glass transition temperature (T_g) for 1 hour exhibits excellent enhanced hardness and compressive strength. Zhao et al. [11] found that the anti-wear property of $Zr_{61}Ti_2Cu_{25}Al_{12}$ MG can be tuned by controlling different degrees of structure relaxation through thermal treatment. In addition to the effect of structure relaxation, the change of surface chemistry (e.g., oxidation) upon dry friction or a simple thermal treatment can also contribute to the tribological performance [12–14]. Once chemical reactions with oxygen are induced by friction heat at the contact surface, the oxidized tribolayer on the surface may act as a solid lubricant and effectively reduce friction and wear [15,16]. Specifically, Fu et al. [17] demonstrated that this oxidized tribolayer could reduce the friction coefficient of $Zr_{41.2}Ti_{13.8}Cu_{12.5}Ni_{10}Be_{22.5}$ MG by ~25%. Jin et al. [18] found that a thin thermal-oxidized layer formed on the $Zr_{42}Ti_{15.5}Cu_{14.5}Ni_{3.5}Be_{24.5}$ MG at $0.83T_g$ would reduce its wear volume by ~34%. Zhou et al. [19] detected an almost 29% reduction in friction coefficient of $Zr_{50}Ti_2Cu_{38}Al_{10}$ MG after thermal treatment, ascribing to the formation of oxidized layer on surface. Salehan et al. [20] also reported that the synergistic effect of the structure relaxation and a dense oxide layer would act concurrently to enhance the wear resistance of an annealed $Zr_{60}Cu_{10}Al_{15}Ni_{15}$ MG. Therefore, wear mechanisms of MGs are closely related to these two factors (structure and oxidation) [21].

* Corresponding authors.
E-mail addresses: zhouqing@nwpu.edu.cn (Q. Zhou), haifengw81@nwpu.edu.cn (H. Wang).
[1] These authors contributed equally.

https://doi.org/10.1016/j.actamat.2022.117934
1359-6454/© 2022 Acta Materialia Inc. Published by Elsevier Ltd. All rights reserved.

However, existing researches regarding the oxidation effect on the tribological behavior of MGs are mainly explored by macroscopic wear tests [17–21], in which the structure effect of the subsurface material cannot be excluded. Atomic force microscope (AFM) has gained global acceptance for probing the fundamental friction mechanisms at nano-scale (e.g., micro-plasticity and surface interaction in metals) [22–24]. More importantly, AFM experimental technology can intrinsically explore the surface-dominated events due to the nano-scale nature of the probed region. For example, Yu et al. [25] proposed the homogeneous plastic flow mechanism of Pt-based MG during AFM nanoindentation, in which only several tens of atoms at surface are evolved in the deformation. Ketov et al. [26] quantitatively investigated the material softening of Zr-Cu-Co-Al MG nearby a surface shear band using AFM. Ross et al. [27] clarified the stress-induced structural evolution in $Zr_{50}Cu_{40}Al_{10}$ MG, with its local heterogeneities clearly revealed by the nanomechanical response of AFM. Moreover, Ko et al. [28] compared the wear resistance of three different FCC metal surfaces based on the microscale topography images and friction behavior by means of AFM. Given the extraordinary detect resolution of the nano-scale probe region, AFM is able to distinguish between the effects of surface structure and chemistry on the wear mechanisms of MGs.

In this work, the effects of structure relaxation and surface oxidation on the nanoscopic wear resistance of the $Zr_{63.6}Cu_{18}Ni_{10.4}Al_8$ MG were investigated. The chosen Zr-based MG has promising applications in micro-electromechanical system (MEMs) owing to its superior mechanical properties and nanoscale thermoplastic formability [29–31]. Especially, the surface forces such as friction cannot be ignored as the size of devices shrinks to micro- or nano-scales [32–34]. Here, we synthesized the MG and then annealed it in atmospheres of argon and oxygen using differential scanning calorimetry (DSC). AFM indentation and nanotribological tests were carried out using the force curve and the lateral force modes to investigate the MG with different surface states. Moreover, molecular dynamics (MD) and ab initio molecular dynamic (AIMD) simulations enabled us to reveal the surface interaction and the friction reduction mechanism after the introduction of O atoms. We found that the synergistic effect of chemical modification and mechanical strengthening contributes to a distinguished tribological performance of the oxidized surface over the structure relaxed sample. Theoretical modeling reveals that O hinders the interfacial bonding and reduces the ploughing friction between the tip and MGs, which underpins the superior wear resistance of the oxidized sample. This finding would not only help to clarify the different wear mechanisms in MGs, but also be crucial to achieve greater flexibility in designing wear-resistant surfaces.

2. Experiments

2.1. Materials

The cylindrical rods (ϕ 3 × 50 mm) of $Zr_{63.6}Cu_{18}Ni_{10.4}Al_8$ MG were fabricated by arc melting in a Ti-gettered argon atmosphere and copper mold suction casting at ambient temperature. Columnar specimens with a height of 3 mm were cut from the rods by a diamond wire saw. Sample surfaces were carefully polished to a mirror finish (RMS roughness was ~2.5 nm) and stress removed. Subsequently, specimens were annealed using differential scanning calorimetry (DSC, NETZSCH) at 550 K (T_g = 647.4 K) for 3 h in argon and oxygen atmospheres. The as-cast, relaxed and oxidized samples are respectively denoted as the AC, RE and OX samples in the following.

The microstructure of specimens was verified using X-ray diffraction spectrometer (XRD, Bruker D8) and transmission electron microscopy (TEM, FEI Talos F200X). Thermodynamic properties were determined by DSC in a pure argon atmosphere at a heating rate of 0.33 K/s. The chemical states of the sample surface were measured by X-ray photoelectron spectroscopy (XPS, VersaProbe III).

2.2. AFM tests

Nano-hardness distribution and nano-tribological tests were carried out via AFM (Asylum, MFP3D). The adopted silicon probes were coated with a diamond-like carbon (Budget Sensors, Tap300DLC) and the nominal radius is 12 ± 3 nm. Before the indentation test, the normal spring constant K_N of the cantilever in this work was calibrated as 48.51 N/m by thermal noise vibration [35], and the sensitivity S was calculated to be 118.13 nm/V by fitting the unloading force curves [36]. The normal force could be formulated via converting voltage signals into forces according to $F_N = K_N S V_N$, with V_N being the normal voltage of photodiode [28]. The nano-hardness was obtained by fitting the force curves with the method of Oliver and Pharr [37]. A loading force of 500 nN was used to evenly distribute 30 × 30 indentation dots in a spatial area of 2 × 2 μm^2 for all samples. Each indentation was maintained on the surface for 1 s to ensure the load stability. However, due to the existence of polishing defects such as surface scratches, the mean value of each sample was counted with dead pixels removed.

In the nano-tribological test, the lateral force F_L could be obtained by converting the voltage using the following equation:

$$F_L = \frac{3}{2} K_L \frac{h}{l} S V_L \tag{1}$$

where V_L is the lateral voltage of the photodiode and the lateral spring constant K_L is 1204.71 N/m. The more detailed method for calculating K_L could be found elsewhere [28]. The height of tip h and the length of cantilever l were measured optically to be 17 μm and 125 μm, respectively. For each sliding test, the friction force could be expressed as:

$$F_f = \frac{F_{L,forward} - F_{L,backward}}{2} \tag{2}$$

where $F_{L,forward}$ and $F_{L,backward}$ are the lateral forces of the cantilever recorded during reciprocating sliding. In this work, we adopted a multi-pass method with the normal load increasing stepwisely during the nano-wear testing, as schematically shown in Fig. 1. The normal force was increased from 78.81 nN to 2960.36 nN in a total number of 16 passes over an area of 2 × 2 μm^2. During this period, the normal force was kept constant and the probe slid back and forth for 18 cycles at a speed of 1 μm/s at each step. Thereby, the topography and friction images were successively recorded under the contact mode. After the test, the topographical variations of the testing area were further scanned by tapping mode with a load of 78.81 nN using the silicon nitride probe, which has a radius of 7 nm and a normal spring constant of 2.62 N/m (Oxford, AC240TS-R3). The wear volume was determined by integrating the wear depth from the cross-sectional profiles over the same area.

2.3. Computation methods and models

2.3.1. MD simulation

In order to reveal the friction mechanism, MD simulation of the interaction between the diamond probe and samples was carried out in a large-scale parallel atom/molecule simulator (LAMMPS). A set of ZrCuNiAl quaternion embedded atom method potential established by Zhou et al. [38] was exploited, and the atomic interactions between carbon, oxygen and metallic atoms were represented by the Lennard-Jones (L-J) potential [39–42]. The as-cast MG (AC) model was obtained by cooling the initial amorphous model of $Zr_{63.6}Cu_{18}Ni_{10.4}Al_{8.0}$ from 2300 K to 300 K at a rate of

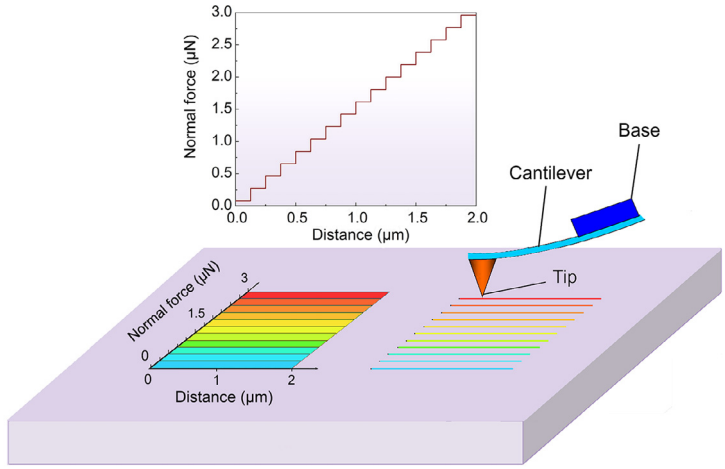

Fig. 1. Schematic diagram of the stepwise multi-pass loading mode during a nano-wear process.

20 K ps^{-1}. Subsequently, the model was heated to 750 K at a rate of 20 K ps^{-1}, relaxed at this temperature and then slowly cooled to 300 K at a rate of 0.5 K ps^{-1} to prepare the relaxed MG (RE) model. Finally, the oxidized amorphous (OX) model was established by following the experimental compositions of oxidized layer (i.e., $Zr_{36.8}Cu_{7.4}Al_{5.6}O_{50.2}$ as shown in what follows). On this basis, the interaction between the diamond and different MG surfaces was approximately evaluated. The specific parameters related to the models and L-J potentials were shown in Table. S1.

2.3.2. AIMD simulation

To further clarify the role of oxidation in the friction reduction, AIMD simulation was conducted to produce the RE and OX models. The total energy calculations were implemented by VASP based on the density functional theory (DFT) [38,43]. The generalized gradient approximation (GGA) with the Perdew-Burke-Ernzerhof (PBE) formulation was used as the pseudopotential potential [44]. The projected augmented wave (PAW) potentials were selected to describe the ionic core interactions [45,46]. Moreover, the periodic boundary condition was applied to all systems and the steps for producing the interface structure were present in Fig. S1. All dynamical simulations were carried out in a canonical ensemble (NVT) through Nosé thermostat to control temperature [47]. The time-step was set as 1 fs. Additionally, the partial density of state (PDOS) for explaining the effect of oxidation on adhesion between the diamond and different MG surface was calculated.

3. Results

3.1. Microstructures

The XRD patterns of as-cast and annealed $Zr_{63.6}Cu_{18}Ni_{10.4}Al_8$ MGs are exhibited in Fig. 2a. The similar broad diffraction peaks reveal that the amorphous nature remains unchanged after annealing below T_g in the atmosphere of either argon or oxygen, as no other sharp peaks exist. However, the DSC curves in Fig. 2b show distinct differences among different samples. All MGs display an endothermic glass transition event and a following exothermic process due to crystallization. The temperature interval of supercooled liquid region (defined as $\Delta T = T_x - T_g$, where T_g is the glass transition temperature, and T_x is the crystallization temperature) decreases obviously for RE and OX samples when compared with the AC sample, suggesting that the thermal stability has been deteriorated. The magnified view of the area represented by the dashed rectangle (inset in Fig. 2b) reveals that the relaxation enthalpy (ΔH), i.e., the exothermic area over a wide temperature range below T_g, distinctly decreases from ~8.51 J/K for the AC sample, to ~6.24 J/K for the RE sample, and then to ~5.84 J/K for the OX sample. It is generally recognized that the relaxation enthalpy is proportional to the amount of free volumes existed in MGs [48,49]. Therefore, upon annealing in an oxygen atmosphere, the dense oxidized layer may promote annihilation of free volumes at the surface of MGs because of the introduction of O.

The structures and composition of oxidative surface are further analyzed by using cross-sectional TEM. Fig. 3a shows the bright field image of TEM, which can be clearly divided into three regions: I) the MG matrix; II) the amorphous oxidized layer on the surface of MG; III) the platinum protective layer. The thickness of amorphous oxidized layer on the OX sample is measured to be 29.6 nm, which is much thicker than the reported natural oxidized layer formed on the Zr-based MG (less than 1 nm) [1]. The corresponding EDS mappings of all elements are displayed in Fig. 3b. It shows that the main components of the layer are the oxides of zirconium, aluminum and copper, which can be also confirmed by the XPS test in Fig. S2. The sectional high-resolution TEM image and the corresponding selected area electron diffraction (SAED) pattern are presented in Fig. 3c. For the MG matrix, only the typical amorphous disordered structure is detected, showing a diffused halo presented in the SAED pattern. For the oxidized layer, it still maintains the amorphous structure although minor crystal phases can also be detected as shown in Fig. 3d. The corresponding fast Fourier transform (FFT) and inverse fast Fourier transform (IFFT) images are shown in the Fig. 3d_1 and Fig. 3d_2. The 2.12 Å-spaced lattice fringes of the nanocrystal phases in Fig. 3d_2 could correspond to {200} of Cu_2O. In view of the limited size (5 nm) and number of crystallized oxides, it is unachievable to detect them in XRD and the crystal particles may have a negligible effect on the properties of the amorphous oxidized layer. Moreover, compared with the MG matrix, only Zr, Cu and Al elements are involved in the amorphous oxidized layer with compositions of $Zr_{36.8}Cu_{7.4}Al_{5.6}O_{50.2}$. As Zr, Al and Cu have lower electronegativities and ionization potentials than Ni, these elements are more reactive in forming bonds with O element. Additionally, the affinity between O and Zr or Al is stronger than that between O and Cu (the heats of formation for ZrO_2, Al_2O_3 and Cu_2O are −1101.3, −1678.1 and −166.7 kJ/mol, respectively [19]), resulting in the relative depletion of Cu on the upmost surface layer when compared with other elements (Fig. 3b).

3.2. AFM indentation test

The surface topography before AFM indentation and subsequent hardness distribution are displayed in Fig. 4. As shown in Fig. 4*a*–*c*, three random sites with the same size (2 μm × 2 μm) are scanned

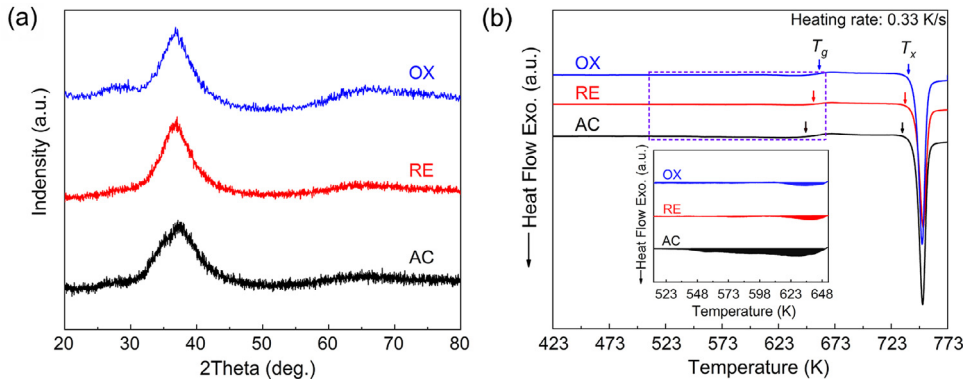

Fig. 2. (a) XRD patterns and (b) DSC curves of as-cast and annealed MGs.

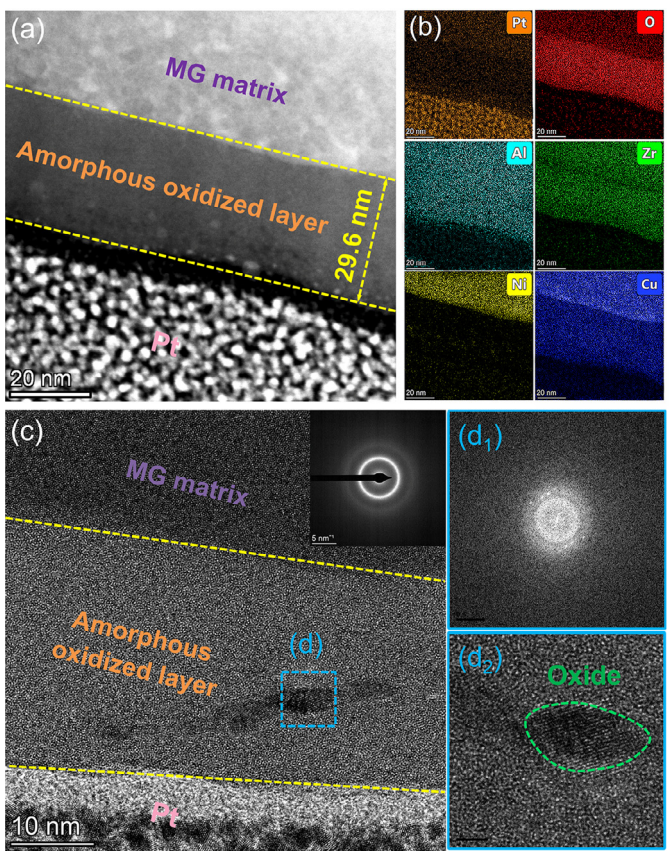

Fig. 3. Structure and composition analysis of the cross-sectional amorphous oxidized layer on the MG surface. (a) The bright field images. (b) The EDS elemental maps corresponding to the analysis region in (a). (c) High-resolution TEM image of surface layer and the corresponding SAED patterns. (d) High-resolution image of a crystalline in the amorphous oxidized layer and the corresponding (d_1) fast Fourier transform (FFT) and (d_2) inverse fast Fourier transform (IFFT) images.

in a tapping mode to characterize the morphology of the three different samples. For these mapped areas, the root-mean-square (RMS) roughness for AC, RE and OX samples are measured to be 1.91, 2.52 and 2.44 nm, respectively. AFM hardness distribution for different samples is further determined from the force curves over the same area as shown in Fig. 4*d–f*. To keep the indentation depth within the oxide layer, the loading force is set as 500 nN with a maximum depth of 15.39 nm. The statistical analysis of the data (insets in Fig. 4*d–f*) shows the mean values of hardness are 8.92, 9.46 and 11.50 GPa for the AC, RE and OX samples, respectively.

The difference in hardness among the three different kinds of samples indicates the variation of structure after thermal treatment. An equation of the relationship between hardness and free volumes of MGs is expressed as [50]:

$$H = C_1 T \sinh^{-1}\left[C_2 s \exp\left(\frac{\Delta E}{C_B} + \frac{s v_c}{v_a}\right)\right] \tag{3}$$

where C_1 and C_2 are the constants, T and h are the temperature and depth of indentation, s is the shear strain rate, ΔE is the activation barrier energy of flow defect, C_B is the Boltzmann's constant, v_a is the average free volume per atom, and v_c is the critical free volume for atom diffusional jumps. Hence, it is noted that the hardness of MG should be inversely proportional to the amount of free volumes when the loading rate of indentation is fixed. The increasing hardness of RE is consistent with the result of reducing free volumes represented in Fig. 2. Once the free volume is annihilated after annealing, there is no enough space in the MG for atomic rearrangement and shear deformation, therefore plastic yielding is postponed. Meanwhile, the maximum hardness of the OX sample indicates that the dense amorphous oxidized layer is harder than the relaxed MG substrate. Similar results have also been reported for the $Zr_{55}Cu_{30}Al_{10}Ni_5$ MG, whose hardness was significantly improved after oxidation [14]. This enhanced surface hardness is expected due to the strong bonding between metallic elements and oxygen.

3.3. Nano-wear test

3.3.1. Critical force for elastic recovery and plastic deformation

Fig. 5 shows AFM topographies of three types of samples under a contact mode before and after the nano-wear test. The RMS roughness over the scanned area of 2 × 2 μm^2 is 2.11, 2.43 and 2.14 nm for the AC, RE and OX samples, respectively (Fig. 5a_1, b_1, c_1). During wear, the normal force increases in a stepwise manner from ~0.1 μN to ~3.0 μN. The variational height and friction signals are obtained synchronously based on the in-situ AFM test system. The surface topography of AC sample (Fig. 5a_2) changes significantly, indicating a wide range of wear occurred on the surface. For the RE sample as shown in Fig. 5b_2, the initial topography is retained after the wear tests with a small normal force (bottom part of the image), whereas, wear occurs when the normal force is large (top part of the image). The wear-less phenomenon is more distinct on the surface of OX sample (Fig. 5c_2), in which most of the initial topography can be identified after the wear test. In this case, wear occurs at a large normal force when compared with the RE sample. The variations of surface profile before and after the wear test indicated along the black and red arrows are further quantified in Fig. 5a_3, b_3, c_3. The initial surface profiles (black lines) with the fluctuation less than 3 nm suggest the relatively flat and

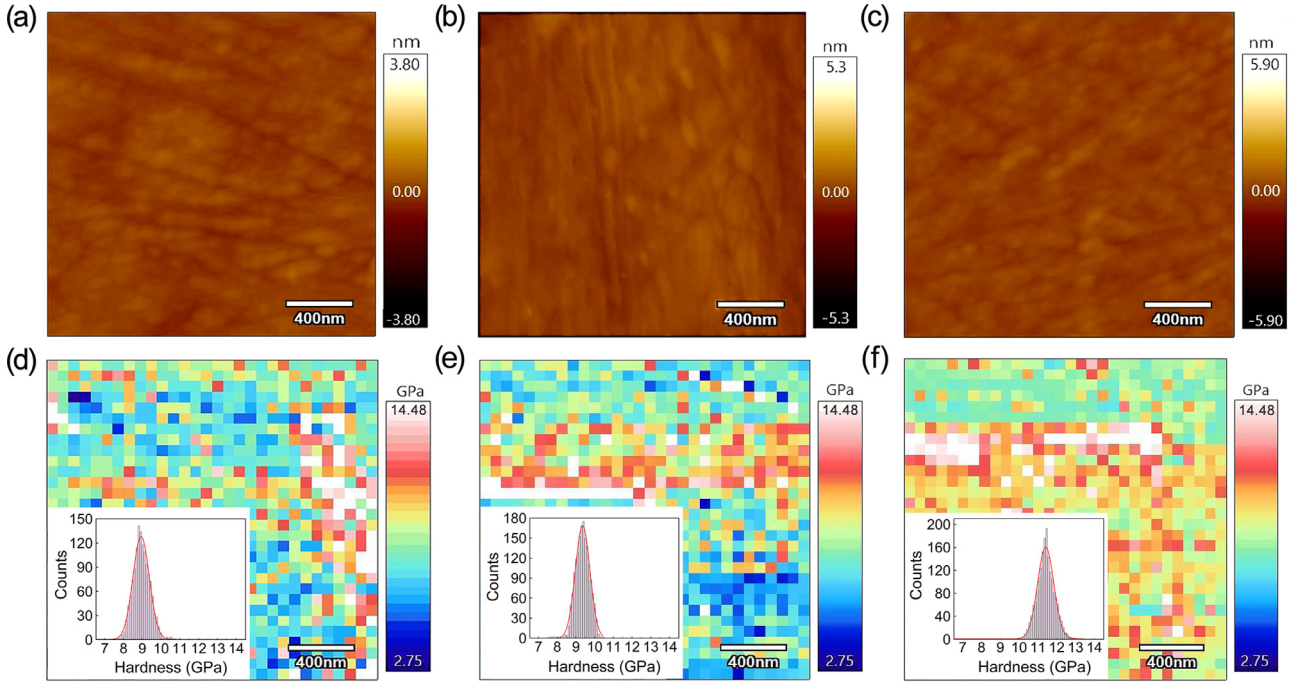

Fig. 4. Surface topography and hardness distribution of different samples. (a, d) AC. (b, e) RE. (c, f) OX.

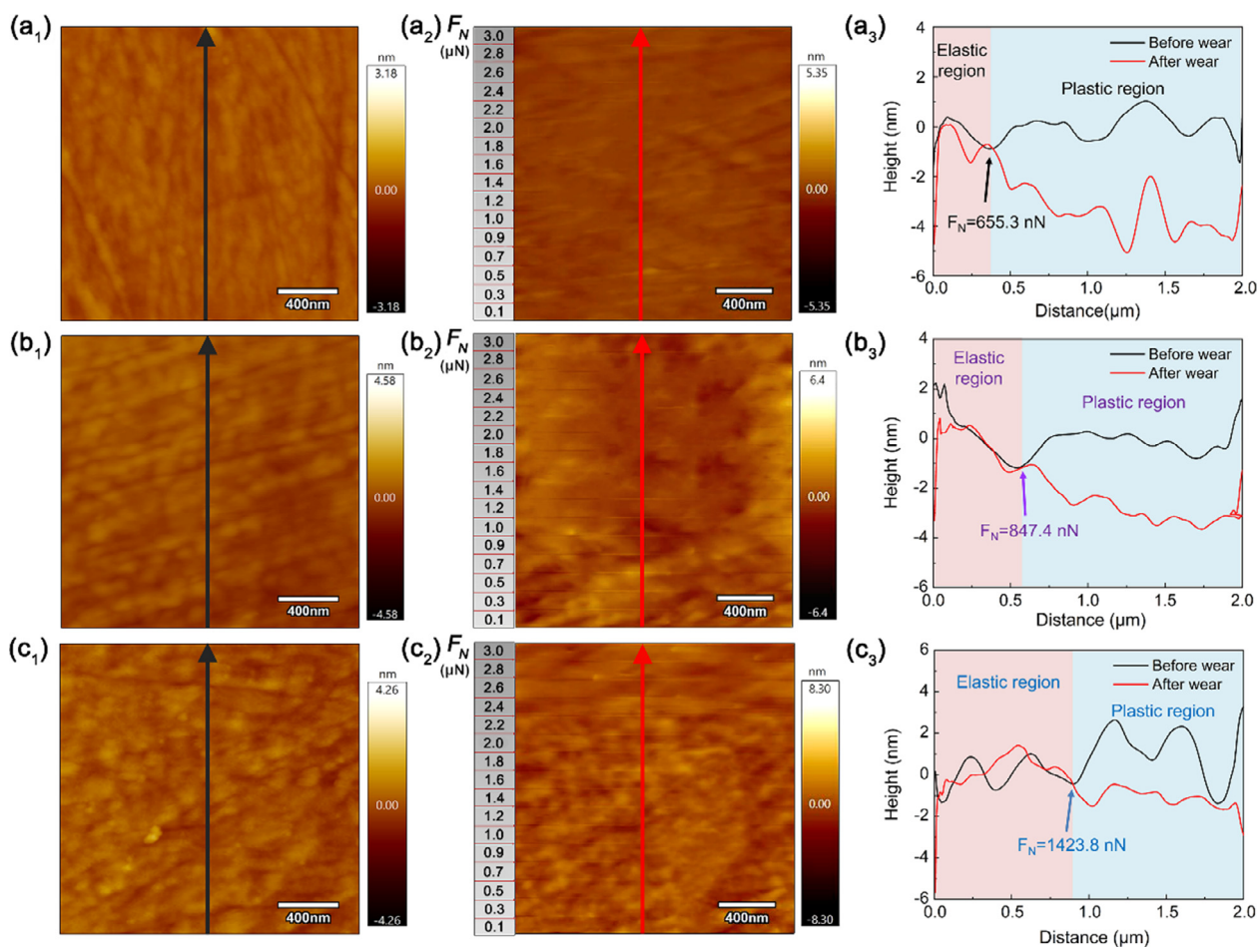

Fig. 5. AFM height images before and after the tribological test. (a_1, b_1, c_1) Height topography images of the AC, RE and OX samples before the wear test. (a_2, b_2, c_2) The corresponding surface profiles after the wear test. The direction of the arrows indicates an increasing normal force for the step-wise nano-tribological test. (a_3, b_3, c_3) The variation of height profile with the sliding distance for the cases of before and after the tribological test. The critical forces corresponding the "elastic-plastic transition" are marked for different samples.

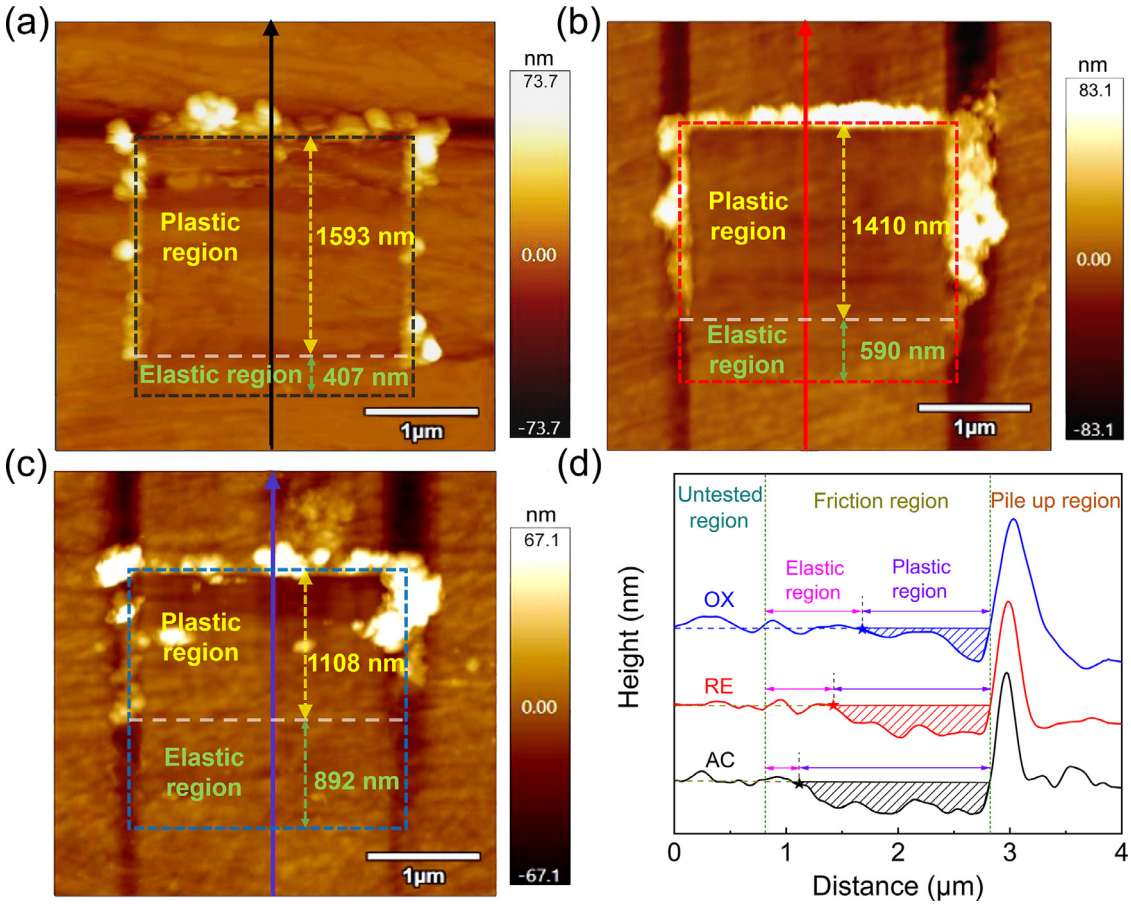

Fig. 6. The AFM surface topographical images of the (a) AC, (b) RE and (c) OX samples after the wear test. (d) The cross-section profiles of wear tracks in different samples.

smooth testing areas. For the surface after wear (red lines), as the normal force increases stepwisely with the increasing distance, the height profile drops nonlinearly after a horizontal fluctuation, and finally reaches the maximum values of ~5.2, ~3.8 and ~2.3 nm for the AC, RE and OX samples, respectively.

In the wear-less region, it is recognized that, the height profile after the wear test is roughly the same as that before the test due to the elastic recovery of the surface. However, the profile after wear gradually disparts from that before wear as the normal force increases, indicating the occurrence of irreversible plastic deformation and wear on the surface. The critical normal force for the "elastic-plastic transition" indicates the onset of plastic deformation, which are given as 655.3, 847.4 and 1423.8 nN for the AC, RE and OX samples, respectively. The significantly increased force for inducing plasticity deformation indicates that the elastic recovery is enhanced considerably in the OX sample, which is in accordance with the general believing that oxides exhibit much higher elastic modulus due to the strong bonding between oxygen and metallic atoms [51].

In the wear region, the damage mechanism transforms from elastic to plastic deformation. To quantitively explore the wear conditions of different samples, the AFM tapping mode was used to scan the wear tracks over a larger area of 4 × 4 μm^2 with a silicon nitride tip. The surface wear topography and the cross-section profile after the wear test are shown in Fig. 6. All scars are characterized by two distinct domains, i.e., the bottom part as the elastic region and the top part as the plastic region. It is noted that all of the worn surfaces demonstrate a similar feature, namely a wear scar with some pileups of materials on the lateral and end sides, indicating the presence of ductile plowing on the surface. The length of both regions for the AC sample is further determined to be 407 nm and 1593 nm, respectively, as shown in Fig. 6a. After performing the same analysis for the RE and OX samples in Fig. 6b, c, the lengths of elastic region are measured as 590 nm and 892 nm, and that for the plastic regions are 1410 nm and 1108 nm, respectively. The corresponding critical normal forces of "elastic-plastic transition" are 655.3, 847.4 and 1423.8 nN, which are consistent with the results shown in Fig. 5. Fig. 6d shows the cross-section profile of wear tracks, including the untested, friction and pile-up regions obtained along the arrows in Fig. 6*a*–*c*. By integrating the wear depth in the friction regions, the wear volumes of AC, RE and OX samples are calculated as 0.012, 0.010 and 0.0024 μm^3, respectively.

For nano-wear test conducted by AFM, the wear rate (W), defined as the wear volume (V) per unit sliding length, is calculated as [24,31,52]:

$$W = \frac{V}{x} \tag{4}$$

The wear-less regime, which is dominated by elastic deformation, is precluded from the corresponding calculation due to the negligible wear rates. Based on Eq. (4), the wear rate of different samples at various normal forces is plotted in Fig. 7. The wear coefficient (k_w) is obtained as the slop of the curve and the wear resistance (R_w) is the reciprocal of wear coefficient as $R_W = 1/k_w$ [52].

The wear rates basically increase with increasing normal force and eventually reach the values of 48.81, 30.02 and 10.01 nm^2 at 3 μN for AC, RE and OX samples, respectively. In comparison with the AC sample for which the k_w is 10.50 nm^2/μN, it is reduced to 8.14 and 0.78 nm^2/μN for RE and OX samples, respectively. The

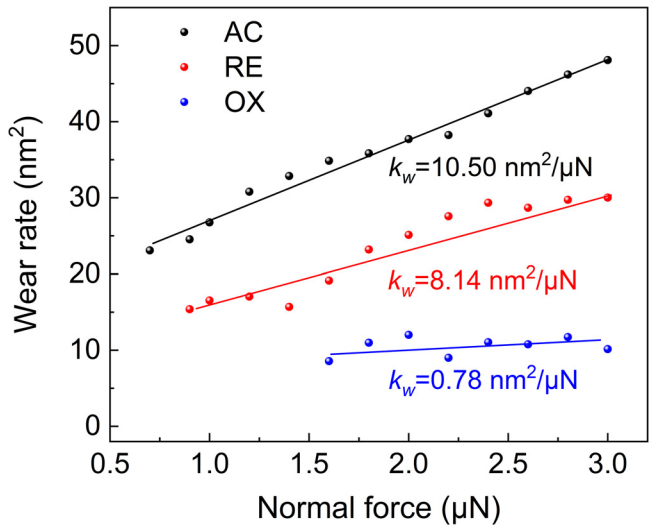

Fig. 7. The wear rate against normal force and the wear coefficient for different samples.

wear rate and wear coefficient of OX samples are far lower than the other two MGs, indicating the positive effect of oxidation on reducing wear. Additionally, the coefficients of wear resistance for AC, RE and OX samples at 1.6 μN are 4.64×10^{10} Pa, 8.35×10^{10} Pa and 1.87×10^{11} Pa, respectively. It's obvious that oxidation leads to an order of magnitude increase in wear resistance for present Zr-based MG, which is much higher than previously reported oxidized Ti-based and Mg-based MGs [31].

3.3.2. Analysis of friction signals during wear

Fig. 8*a*–*c* display the variation of friction voltage with the normal force for different samples. Here a more positive voltage signifies higher friction during the tests. By comparing the maximum value of friction signals, it can be noted that the OX sample has the minimum value under the same load. Specifically, the profile of normal and friction forces along the vertical lines in Fig. 8*a*–*c* is given in Fig. 8*d*–*f*. The friction force increases nonlinearly with the increase of normal force, indicating the existence of load-dependent friction coefficients in different regions.

To clarify the friction mechanism, the friction coefficient is further calculated based on the correlation between the friction force and the normal force, as shown in Fig. 9*a*–*c*. The friction force increases with the normal force but shows two different slopes for all samples. Here, the traditional Amonton's law for calculating the friction coefficient is no longer applicable due to the nonnegligible adhesion force at nanoscale [53]. According to Bowden and Tabor [54], the friction force is the sum of the shearing force associated with adhesion, F_1, and the ploughing force accompanied by plastic deformation, F_2, i.e., $F_f = F_1 + F_2$. It's true that the friction force is positively correlated with the normal force in both elastic and plastic regions. In the elastic region, since the ploughing force F_2 is 0, the shearing friction coefficient μ_1 can be determined from the linear slope of the plot of the friction force against the normal load. In the plastic region, the total friction coefficient μ corresponds to the synergistic effect of shearing and ploughing, and in this case the ploughing coefficient μ_2 can be obtained as the difference between the total friction and shearing coefficient as $\mu_2 = \mu - \mu_1$. This load dependence of friction coefficient is therefore responsible for the slope change. For all samples, wear can be observed in the plastic region when the slope becomes deeper. Therefore, it can be clearly identified in Fig. 9*a*–*c* that the critical force for the elastic-plastic transition (the point at which the slope changes) of the RE and OX samples increases successively, which is consistent with the results in Figs. 5 and 6.

The respective friction coefficients for shearing and ploughing determined above are shown in Fig. 9d. It is noted that the ploughing coefficient μ_2 decreases continuously from the case of AC and RE to the case of OX; the shearing coefficient μ_1 increases from the case of AC to that of RE but decreases significantly in OX. In the plastic/wear region, the total friction coefficient μ decreases significantly from 0.0293 and 0.0279 for MGs with different structure states to 0.0034 for the oxidized sample. Accordingly, it's concluded that the anti-wear properties of Zr-based MG could be enhanced when annealed in both argon and oxygen atmospheres. Particularly, the friction coefficient and wear volume of OX sample decrease tremendously, indicating that oxidation plays a more significant role in the wear reduction of MGs than structure relaxation.

4. Discussion

Based on the above results, the oxidized Zr-based MG exhibits the superior anti-wear (the wear loss reduced by 80%) and anti-friction (the friction coefficient reduced by 88%) performance. Obviously, the lubrication effect and friction reduction induced by oxidation are more significant in nano-wear tests than that in macroscopic wear tests [17–19]. This is related to the fact that the intrinsic friction properties of surface oxidized layer can only be explored via AFM due to its nano-scale contact region. However, in macroscopic wear tests, the effect of structure relaxation on friction behavior cannot be excluded and the thin oxidized layer only has a limited contribution to enhance the wear resistance of MGs. Consequently, the effective wear resistance of oxidized Zr-based MG surface may provide a guidance for the development of microdevices.

Generally, the analysis of oxidation on macroscopic wear mechanism mainly focuses on the crystalline phases and the mechanical properties of oxide layer [17–21], while the nano-wear tests render the wear mechanism to be revealed from the perspective of shearing and ploughing friction due to its single-asperity contact advantage. The shearing component is intimately related to the interfacial adhesion and the ploughing component is a function of the mechanical response of contact surface. Although a single-asperity contact in nano-wear test may be insufficient to reflect the general macroscopic wear, it clarifies the mechanical interaction between two contacting surfaces, thus providing the insight of potential deformation mechanisms which are helpful to explain the macroscopic tribology phenomenon. Therefore, the distinct effects of structure relaxation and oxidation on wear performance are discussed from adhesion and ploughing aspects separately as follows.

4.1. Adhesion effect

Fig. 10 shows the spatial distribution of adhesion force between the diamond tip and the three MGs via AFM indentation. In a typical indentation test, the diamond AFM tip with a maximum load of 500 nN approaches to the sample surface at a constant rate of 500 nm/s and then retracts at the same rate. The force curves are recorded synchronously [55]. Thus, the separation point and adhesion force between the tip and sample surface are characterized from force curves exemplified in Fig. 10a. The adhesion forces of 900 points distributed over an area of 2×2 μm^2 are statistically analyzed and the characteristic values are obtained as shown in Fig. 10*b*–*d*. It is noted that the mean adhesion force increases from the AC sample (20.8 nN) to the RE sample (27.1 nN) but reduces drastically for the OX sample (5.9 nN), showing a similar trend with the theoretical predictions.

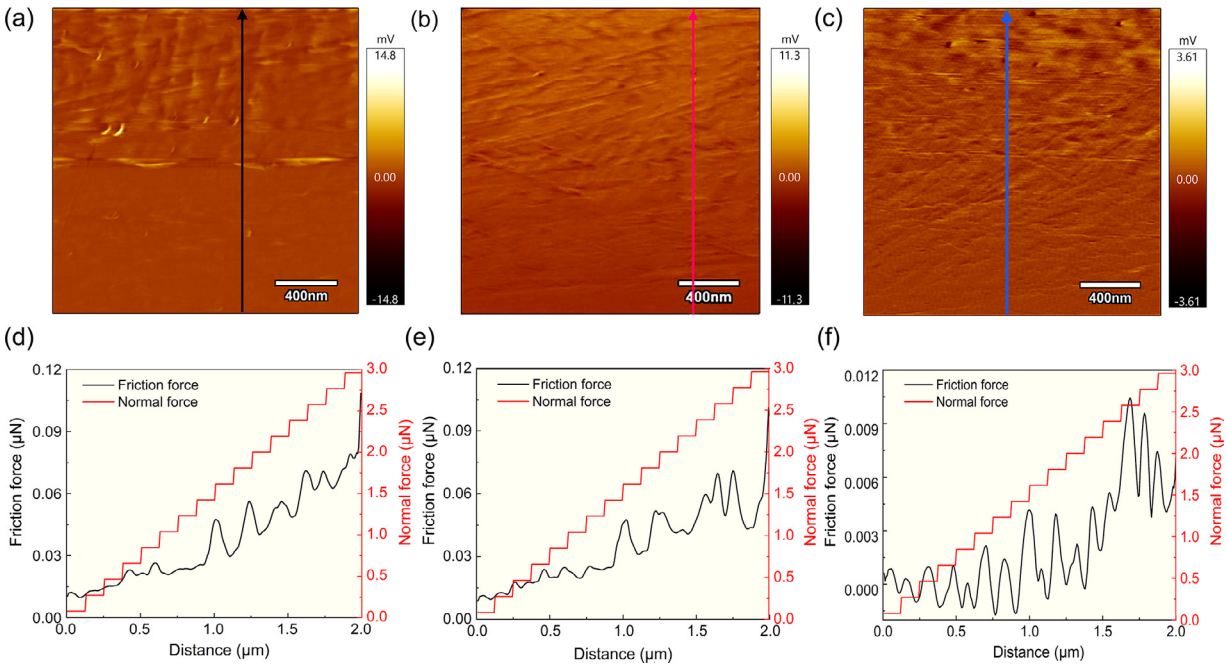

Fig. 8. The images of friction signal and the variation of friction force (with the normal force stepping up) for different samples: (a, d) AC, (b, e) RE and (c, f) OX.

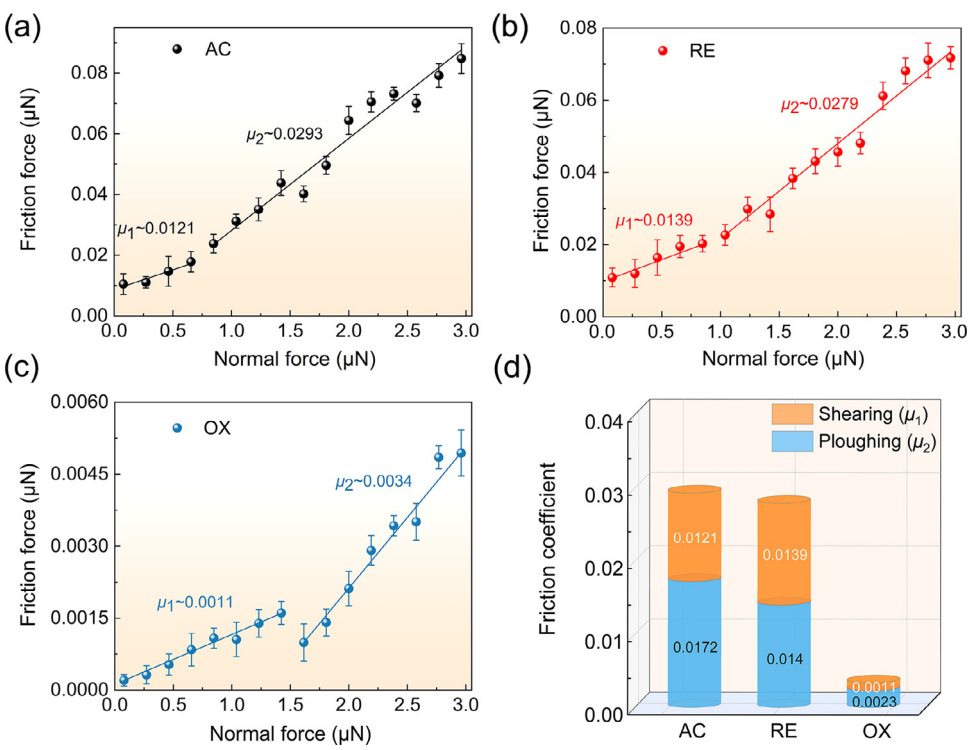

Fig. 9. The friction force as a function of the normal force for different samples: (a) AC, (b) RE, (c) OX. (d) The friction coefficients of shearing and ploughing for different kinds of samples.

In order to reveal the adhesion mechanism, MD simulation was adopted to shed light on the interface interaction. We calculated the energy variation with the separation of two surfaces *d* for three interfaces as shown in Fig. 11*a*–*c*. The reference energy is the total energy of the two fully separated slabs. Hence, a positive change in energy suggests that the two surfaces are mutually exclusive, and a negative value suggests that the tip is attracted to the sample surface with the decreasing interface spacing [56]. The result in Fig. 11d indicates that the interaction between the diamond and the RE surface is slightly enhanced in comparison with that for the AC surface. Therefore, we can conclude that the structure relaxation can somehow strengthen the affinity between the diamond and the MG surface. As the composition is the same for both samples, the difference of adhesion should rely on the variation of structural states. The less free volumes in RE can result in a decreased average atomic volume and an increased atomic packing density, which increases the number of interfacial bonding between the diamond and MG surfaces. This may account for the mi-

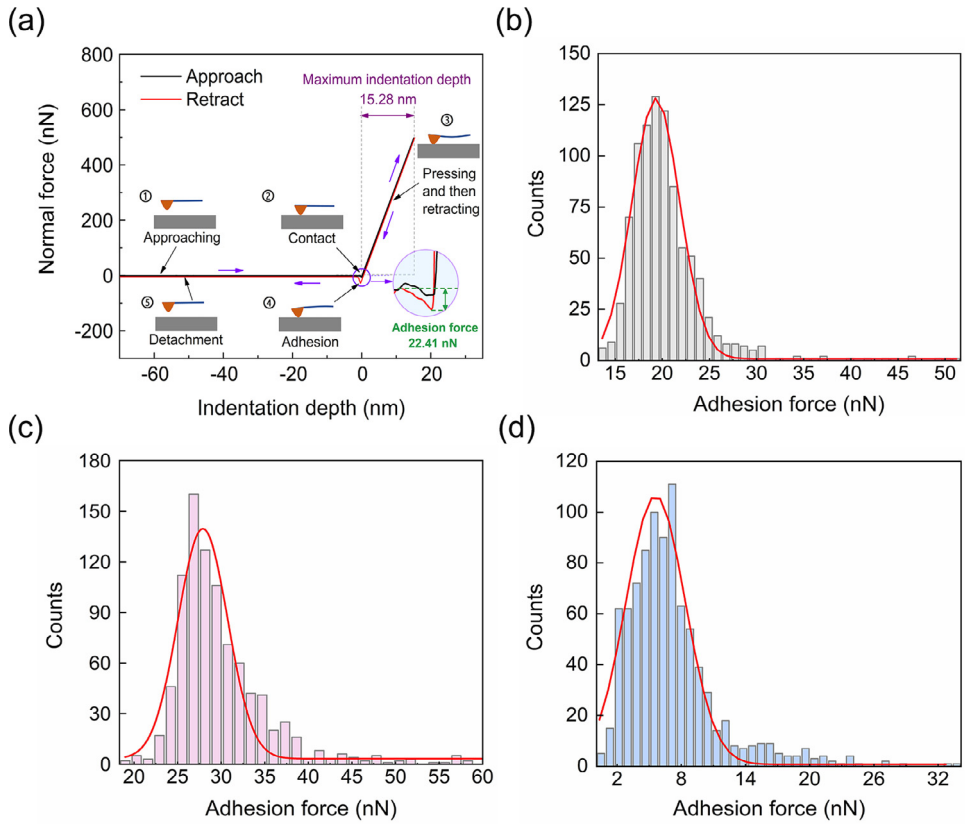

Fig. 10. The adhesion force between the diamond tip and different surface states via AFM indentation. (a) Adhesion measurement and the exemplified force curve. Distributions of the adhesion force for different samples: (b) AC, (c) RE and (d) OX.

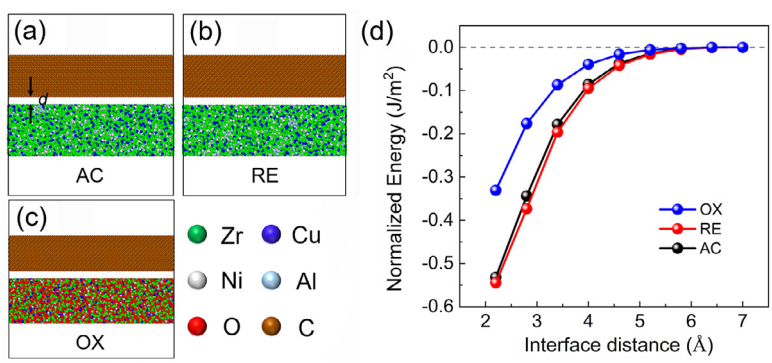

Fig. 11. The three different interface models for (a) AC, (b) RE and (c) OX samples. (d) Plot of the normalized energy versus the interfacial distance for different interfaces.

nor increase of interface adhesion in the RE sample. Although the OX sample possesses a much higher atomic packing density due to the permeation of a large number of small oxygen atoms along with the structure relaxation, it shows a notably lower affinity with the diamond surface. This contradiction can be explained by the change of surface chemical states due to the composition variation in the oxide layer.

Since the L-J atom potentials cannot well capture electron structures and the atomic bonding nature in the complex compositions of oxidized samples, we further calculated the interface binding energies using the ab initio method although our models cannot fully represent complex arrangements of atoms in the amorphous due to the limited simulation size (Fig. S1). The obtained interface binding energies $E^b_{interface}$ between diamond and different samples are given in Fig. 12. Although there is a fluctuation of the value $E^b_{interface}$ for each type of interfaces as their atom configurations are distinct, the averaged $E^b_{interface}$ of diamond/OX (-3.84 J/m^2) is obviously larger than that of diamond/RE (-4.90 J/m^2), which may be attributed to the weakening bonds between diamond and metallic elements after the introduction of O atoms. Generally, a higher binding energy indicates a weaker interaction at the interface [56]. Here, the higher binding energy indicates that oxidation of MG reduces its ability to adhere C atoms, therefore reducing the friction.

In order to understand the effect of introduced O on the adhesion mechanism of diamond/MG interface, we calculated the partial density of state (PDOS) around the Fermi level of the diamond/RE and diamond/OX interfaces. As shown in Fig. 13a, the electron states are mainly from C and Zr atoms, while other atoms (Cu, Ni and Al) have the lower density of electron states. In Fig. 13c, the PDOS of C atoms is enclosed by the PDOS of metallic atoms around the Fermi level (0 eV), which indicates that there

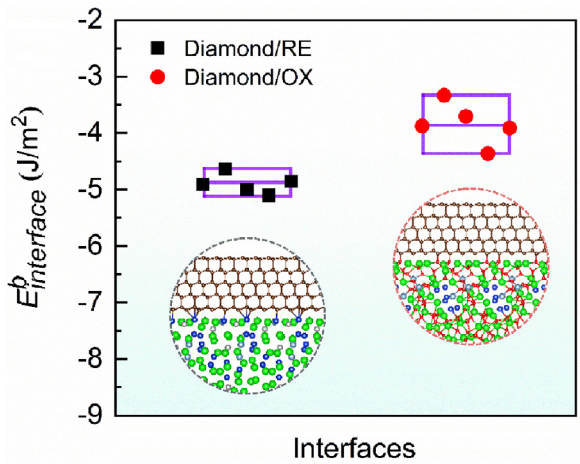

Fig. 12. The interface binding energies$E^b_{interface}$for diamond/RE and diamond/OX.

is a strong interaction between C atoms and metallic atoms at the interface. The obvious orbital hybridization indicates that the interaction between C atoms and metallic atoms mostly has covalent characteristics. This high interaction between C atoms and metallic atoms might be attributed to the fact that the pristine diamond surface has one dangling bond that can hybridize with the vacant orbitals from metallic atoms to form interface bonding [57]. Besides, the carbide forming metallic elements (e.g., Zr) are also found to have a strong adhesion on diamond [58]. On the other hand, the introduction of O results in quite different modification on the electronic structure and interface interaction of MG. As shown in Fig. 13b, the PDOS of O atoms changes at the energy ranging around −22∼−18 eV and −8∼−2 eV, which is corresponding to the *s* and *p* states of O atoms, respectively. In addition, the peaks of Zr atoms show multiple coupling with those of O within these energy ranges of −22∼−18 eV and −8∼−2 eV, introducing strong interactions between Zr-O. Besides, the free electrons in the valence shell of metallic atoms are easily transferred to O due to its larger electronegativity (compared with C) and the MG is passivated by O. This means that the presence of O hinders the metal from forming additional bonding with diamond because no extra electrons are available on the surface. This is reflected by the dramatic decrease of PDOS of metallic atoms at the interface, together with a small overlap area of electronic states between C and MG in Fig. 13d when compared with Fig. 13c. As a result, the interaction between C and MG is significantly reduced, and the diamond on the oxygenated MG shows weakened adhesion strength, being consistent with the experimental results (Fig. 10).

4.2. Ploughing effect

The ploughing during wear mainly derives from the resistance to plastic deformation. Considering a same flow stress in both lateral and normal directions, the ploughing coefficient μ_2 is then determined by an area ratio of A_l/A_n, where A_l and A_n are the contacted area between the tip and surface in the two directions. In addition, elastic recovery of the surface at the rear part of tip can increase the contacted area A_n at the normal direction, therefore reducing the ploughing coefficient. Lafaye et al. [59] obtained an equation for the ploughing coefficient as:

$$\mu_2 = \frac{2}{a^2} \cdot \frac{\beta^2 \cdot \sin^{-1}(a\cos w/\beta) - \sqrt{R^2 - a^2} \cdot a\cos w}{\pi + 2w + \sin 2w} \tag{5}$$

Here $a = \sqrt{2hR - h^2}$ is the contact radius, R is the radius of the tip and h is the penetration depth. Accounting for the elastic recovery, $w = \sin^{-1}\sqrt{2H(R-h)/aE_r}$ is the rear angle. H and E_r are the hardness and reduced modulus of the sample, $\beta = \sqrt{R^2 - a^2\sin^2 w}$ is considered as a fictive radius of the tip.

Based on Eq. (5), it is noted that a shallower penetration depth h generally leads to a lower μ_2 [60]. For the RE sample with structure relaxation, which has lower free volumes and higher hardness than the AC sample, the penetration depth during wear should be shallower at a fixed normal force, thus leading to a lower μ_2. On the other hand, a higher rear angle w (or more elastic recovery) also results in a lower μ_2. Since the OX sample is much harder and has the largest elastic recovery among the three samples, it is expected to have a remarkable reduction in the ploughing coefficient.

Fig. 14 schematically illustrates the wear mechanisms associated with structure relaxation and oxidation. As shown in Fig. 14a,

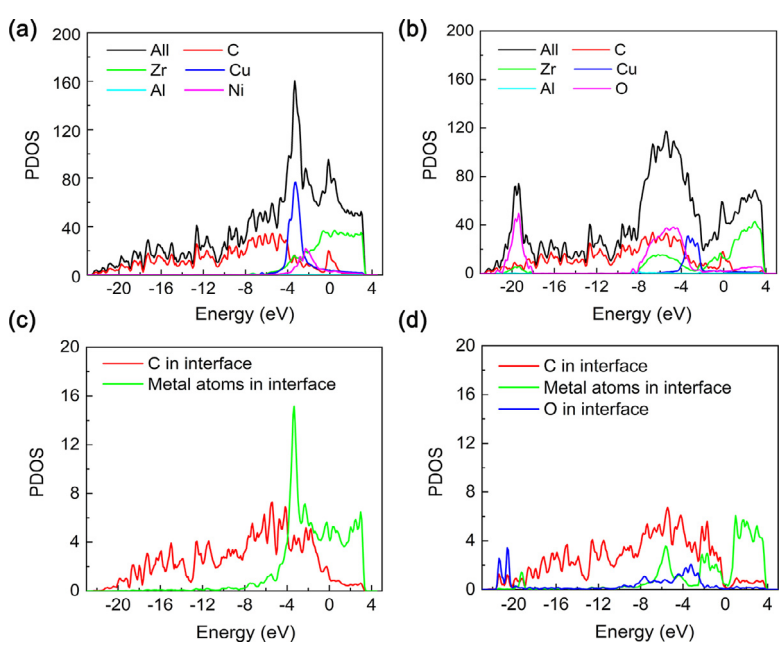

Fig. 13. The partial density of state (PDOS) of (a, c) the diamond/RE and (b, d) diamond/OX interfaces.

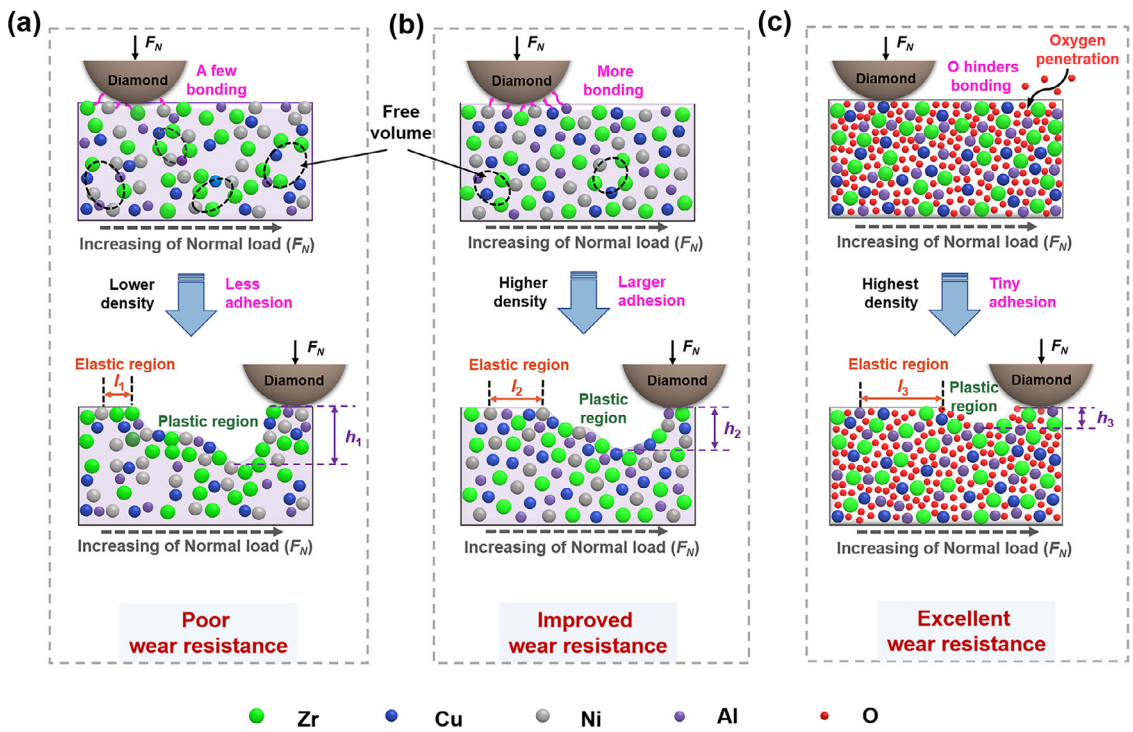

Fig. 14. Schematic diagram of wear mechanisms in different samples: (a) AC, (b) RE and (c) OX.

the as-cast MG possesses abundant free volumes, which exhibits a lower atomic density and results in less bonding between the surface and C atoms. Additionally, the lower hardness and elastic recovery ability are more prone to induce plastic flow, leading to the poor wear resistance of AC sample. Fig. 14b reveals the wear mechanism of the RE sample with structure relaxation after annealing in argon. Compared with the AC sample, the thermal treatment renders a significant decrease of free volumes and an increase of atomic packing density. Accordingly, the elastic recovery ability is enhanced (i.e., the elastic region $l_2 < l_1$ (Fig. 6)), leading to an improved tribological performance for the RE sample (i.e., the wear depth $h_2 < h_1$ (Fig. 5)), although it has a larger interfacial adhesion for the more interatomic bonding. For the OX sample annealed in oxygen, the penetration of oxygen atoms increases the atomic density in the MG and forms a dense amorphous oxidized layer, as shown in Fig. 14c. Although the number of interfacial bonds should increase in the OX sample, the passivation of MG surface by O atoms reduces significantly the interface interaction. The excellent wear resistance is hence obtained ($h_3 < h_2 < h_1$) due to its tiny adhesion, highest hardness and strongest elastic recovery ($l_3 > l_2 > l_1$).

5. Conclusions

In this paper, the effect of structure and oxidation on the $Zr_{63.6}Cu_{18}Ni_{10.4}Al_8$ MG was systematically investigated through nano-wear tests. The wear resistance and friction mechanism of annealed samples in both argon and oxygen atmospheres were analyzed. Compared with the as-cast sample, a larger shearing/adhesive friction for the relaxed MG is derived, whereas, the tremendous reduction of adhesion in the oxidized MG indicates that the introduced O atoms weaken the interaction between metallic atoms and diamond tip. Besides, the reduction of ploughing coefficient is found for MGs after annealing in both argon and oxygen atmospheres, which is mainly attributed to the increased hardness and the stronger elastic recovery ability. Consequently, due to the synergetic chemical modification and mechanical strengthen by O atoms, the oxidized MG exhibits the most distinguished tribological performance, which establishes the superior role of oxidation over structure relaxation during wear. These findings verified the contributions of structural alteration and oxidation behavior played in sliding tests, which may fill the gap between the microscopic friction mechanism and macroscopic wear as well as guide to design the wear-resistant MGs.

Declaration of Competing interest

The authors declare that they have no conflict of interest.

Acknowledgements

This work was supported by the National Natural Science Foundation of China (No. 52175188) and the Fundamental Research Funds for the Central Universities (3102019JC001).

Supplementary materials

Supplementary material associated with this article can be found, in the online version, at doi:10.1016/j.actamat.2022.117934.

References

[1] S.V. Ketov, A.S. Trifonov, Y.P. Ivanov, A.Y. Churyumov, A.V. Lubenchenko, A.A. Batrakov, J. Jiang, D. Louzguine-Luzgin, U. Eckert, J. Orava, A.L. Greer, On cryothermal cycling as a method for inducing structural changes in metallic glasses, NPG Asia Mater 10 (2018) 137–145.
[2] W.H. Zhou, F.H. Duan, Y.H. Meng, C.C. Zheng, H.M. Chen, A.G. Huang, Y.X. Wang, Y. Li, Effect of alloying oxygen on the microstructure and mechanical properties of Zr-based bulk metallic glass, Acta Mater 220 (2021) 117345.
[3] Y. Du, Q. Zhou, Q. Jia, Y. Shi, H. Wang, J. Wang, Imparities of shear avalanches dynamic evolution in a metallic glass, Mater. Res. Lett. 8 (2020) 357–363.
[4] A. Aditya, H.F. Wu, H. Arora, S. Mukherjee, Amorphous metallic alloys: pathways for enhanced wear and corrosion resistance, JOM 69 (11) (2017) 1–6.
[5] A.L. Greer, K.L. Rutherford, I.M. Hutchings, Wear resistance of amorphous alloys and related materials, Int. Mater. Rev. 47 (2) (2002) 87–112.
[6] M.L. Rahaman, L.C. Zhang, H.H. Ruan, Understanding the friction and wear mechanisms of bulk metallic glass under contact sliding, Wear 304 (2013) 43–48.

[7] J. Ketkaew, R. Yamada, H. Wang, D. Kuldinow, B.S. Schroers, W. Drnowski, T. Egami, J. Schroers, The effect of thermal cycling on the fracture toughness of metallic glasses, Acta Mater 184 (2020) 100–108.
[8] Y. Huang, W. Zheng, F. He, J. Shen, The temperature dependent dynamic mechanical response of a ZrCuNiAl bulk metallic glass, Mater. Sci. Eng. A 551 (2012) 100–103.
[9] A. Slipenyuk, J. Eckert, Correlation between enthalpy change and free volume reduction during structural relaxation of $Zr_{55}Cu_{30}Al_{10}Ni_5$ metallic glass, Scripta Mater 50 (2004) 39–44.
[10] Z.Q. Chen, L. Huang, P. Huang, K.W. Xu, F. Wang, T.J. Lu, Clarification on shear transformation zone size and its correlation with plasticity for Zr-based bulk metallic glass in different structural states, Mater. Sci. Eng. A 677 (2016) 349–355.
[11] J. Zhao, M. Gao, M.X. Ma, X.F. Cao, Y.Y. He, W.H. Wang, J.B. Luo, Influence of annealing on the tribological properties of Zr-based bulk metallic glass, J. Non-Cryst. Solids 481 (2018) 94–97.
[12] D. Maddala, R.J. Hebert, Effect of notch toughness and hardness on sliding wear of $Cu_{50}Hf_{41.5}Al_{8.5}$ bulk metallic glass, Scripta Mater 65 (2011) 630–633.
[13] C. Liu, Z. Li, W. Lu, Y. Bao, W. Xia, Reactive wear protection through strong and deformable oxide nanocomposite surfaces, Nat. Commun. 12 (2021) 5518.
[14] M. Zhang, D. Yao, Z.Y. Cao, P. Li, P. Zhou, X.Y. Wang, Influence of oxidation on the performance of $Zr_{55}Cu_{30}Al_{10}Ni_5$ BMG, Intermetallics 79 (2016) 20–27.
[15] D. Luo, Q. Zhou, W. Ye, Y. Ren, C. Greiner, Y. He, H. Wang, Design and characterization of self-lubricating refractory high entropy alloy-based multilayered films, ACS Appl. Mater. Interfaces 13 (2021) 55712–55725.
[16] Q. Zhou, W. Han, D. Luo, Y. Du, J. Xie, X.Z. Wang, Mechanical and tribological properties of Zr–Cu–Ni–Al bulk metallic glasses with dual-phase structure, Wear 474-475 (2021) 203880.
[17] X. Fu, T. Kasai, M.L. Falk, D.A. Rigney, Sliding behavior of metallic glass: part I. Experimental investigations, Wear 250 (2001) 409–419.
[18] H.W. Jin, R. Ayer, J.Y. Koo, R. Raghavan, U. Ramamurty, Reciprocating wear mechanisms in a Zr-based bulk metallic glass, J. Mater. Res. 22 (2007) 264–273.
[19] K. Zhou, C. Chen, Y. Liu, S. Pang, N. Hua, W. Yang, T. Zhang, Effects of lutetium addition on formation, oxidation and tribological properties of a Zr-based bulk metallic glass, Intermetallics 90 (2017) 81–89.
[20] R. Salehan, H.R. Shahverdi, R. Miresmaeili, Effects of annealing on the tribological behavior of $Zr_{60}Cu_{10}Al_{15}Ni_{15}$ bulk metallic glass, J. Non-Cryst. Solids 517 (2019) 127–136.
[21] K. Miyoshii, D.H. Buckley, Microstructure and surface chemistry of amorphous alloys important to their friction and wear behavior, Wear 110 (1986) 295–313.
[22] A. Caron, D.V. Louzguine-Luzguin, R. Bennewitz, Structure vs chemistry: friction and wear of Pt-based metallic surfaces, ACS Appl. Mater. Interfaces 5 (2013) 11341–11347.
[23] S.K. Kwon, H.D. Kim, X.Q. Pei, H.E. Ko, H.W. Park, R. Bennewitz, A. Caron, Effect of cooling rate on the structure and nanotribology of Ag–Cu nano-eutectic alloys, J. Mater. Sci. 54 (2019) 9168–9184.
[24] A. Caron, P. Sharma, A. Shluger, H.J. Fecht, D.V. Louzguine-Luzguin, A. Inoue, Effect of surface oxidation on the nm-scale wear behavior of a metallic glass, J. Appl. Phys. 109 (2011) 5476-151.
[25] J. Yu, A. Datye, Z. Chen, C. Zhou, O.E. Dagdeviren, J. Schroers, U.D. Schwarz, Atomic-scale homogeneous plastic flow beyond near-theoretical yield stress in a metallic glass, Nat. Commun. 2 (2021) 22.
[26] S.V. Ketov, H.K. Nguyen, A.S. Trifonov, K. Nakajima, D.V. Louzguine-Luzgin, Huge reduction of Young's modulus near a shear band in metallic glass, J. Alloy Compd. 687 (2016) 221–226.
[27] P. Ross, S. Küchemann, P.M. Derlet, H. Yu, W. Arnold, P. Liaw, K. Samwer, R. Maaß, Linking macroscopic rejuvenation to nano-elastic fluctuations in a metallic glass, Acta Mater 138 (2017) 111–118.
[28] H.E. Ko, H.W. Park, J.Z. Jiang, A. Caron, Nanoscopic wear behavior of face centered cubic metals, Acta Mater 147 (2018) 203–212.
[29] M.C. Li, M.Q. Jiang, G. Ding, Z.H. Peng, F. Jiang, L. He, J. Sun, The correlation between weakest configurations and yield strength of Zr-based metallic glasses, J. Non-Cryst. Solids 468 (2017) 52–57.
[30] S.J. Kang, K.T. Rittgen, S.G. Kwan, H.W. Park, R. Bennewitz, A. Caron, Importance of surface oxide for the tribology of a Zr-based metallic glass, Friction 5 (1) (2017) 115–122.
[31] D.V. Louzguine-Luzgin, H.K. Nguyen, K. Nakajima, S.V. Ketov, A.S. Trifonov, A study of the nanoscale and atomic-scale wear resistance of metallic glasses, Mater. Lett. 185 (2016) 54–58.
[32] E. Broitman, The nature of the frictional force at the macro-, micro-, and nano-scales, Friction 2 (1) (2014) 40–46.
[33] D.X. Han, G. Wang, J.L. Ren, L.P. Yu, J. Yi, I. Hussain, S.X. Song, H. Xu, K.C. Chan, P.K. Liaw, Stick-slip dynamics in a $Ni_{62}Nb_{38}$ metallic glass film during nanoscratching, Acta Mater 136 (2017) 49–60.
[34] S. Hsu, C. Ying, F. Zhao, The nature of friction: a critical assessment, Friction 2 (1) (2014) 1–26.
[35] H.J. Butt, M. Jaschke, Calculation of thermal noise in atomic force microscopy, Nanotechnology 6 (1995) 1–7.
[36] H.E. Ko, S.G. Kwan, H.W. Park, A. Caron, Chemical effects on the sliding friction of Ag and Au (111), Friction 6 (2017) 84–97.
[37] W.C. Oliver, G.M. Pharr, An improved technique for determining hardness and elastic modulus using load and displacement sensing indentation experiments, Mater. Res. Soc. 7 (1992) 6.
[38] X.W. Zhou, R.A. Johnson, H.N.G. Wadley, Misfit-energy-increasing dislocations in vapor-deposited CoFe/NiFe multilayers, Phys. Rev. B. 69 (2004) 144113.
[39] D. Hua, W. Wang, D. Luo, Q. Zhou, Molecular dynamics simulation of the tribological performance of amorphous/amorphous nano-laminates, J. Mater. Sci. Tech. 105 (2022) 226–236.
[40] L. Xie, P. Brault, A.L. Thomann, L. Bedra, Molecular dynamic simulation of binary Zr_xCu_{100-x} metallic glass thin film growth, Appl. Surf. Sci. 274 (2013) 164–170.
[41] W.L. Jorgensen, J. Chandrasekhar, J.D. Madura, R.W. Impey, M.L. Klein, Monte Carlo thermodynamic and structural properties of the TIP4P water model: dependence on the computational conditions, J. Chem. Phys. 926 (1983) 79.
[42] V.P. Filippova, S.A. Kunavin, M.S. Pugachev, Calculation of the parameters of the Lennard-Jones potential for pairs of identical atoms based on the properties of solid substances, Inorg. Mater: Appl. Res. 6 (2014) 3–6.
[43] G. Kresse, J. Furthmiiller, Efficiency of ab-initio total energy calculations for metals and semiconductors using a plane-wave basis set, Comp. Mater. Sci. 6 (1996) 15–50.
[44] J.P. Perdew, K. Burke, M. Ernzerhof, Generalized gradient approximation made simple, Phys. Rev. Lett. 77 (1996) 3865–3868.
[45] G. Kresse, D. Joubert, From ultrasoft pseudopotentials to the projector augmented-wave method, Phys. Rev. B 59 (1999) 1758–1775.
[46] P.E. Blochl, Projector augmented-wave method, Phys. Rev. B 50 (1994) 17953–17979.
[47] W. Li, C. Hongri, Z. Jingxiang, Medium-range order structure in $Al_{80}Fe_{20}$ alloy during rapid solidification, Phys. Lett. A 301 (2002) 477–483.
[48] W. Guo, Y.M. Shao, J. Saida, M. Zhao, S.L. Lu, S.S. Wu, Rejuvenation and plasticization of Zr-based bulk metallic glass with various Ta content upon deep cryogenic cycling, J. Alloy Compd. 795 (2019) 314–318.
[49] Q. Jia, Q. Zhou, Y. Ren, Y. Du, X. Zhao, X.-.Z. Wang, H. Wang, B.D. Beake, F. Zhou, Tribological characteristics of Ti-based bulk metallic glass via deep cryogenic–cycling treatment, Mater. Charact. 179 (2021) 111356.
[50] N. Li, L. Liu, Q. Chen, J. Pan, K.C. Chan, The effect of free volume on the deformation behaviour of a Zr-based metallic glass under nanoindentation, J. Phys D: Appl. Phys. 40 (2007) 6055–6059.
[51] Y.F. Xu, L.P.H. Jeurgens, L.C. Lin, S. Ma, S.L. Zhu, Y. Huang, Y.C. Liu, J.W. Qiao, Z.M. Wang, Revealing the univariate effect of structural order on the oxidation of ternary alloys: amorphous vs. crystalline Cu–Zr–Al alloys, Corros. Sci. 183 (2021) 109309.
[52] D.V. Louzguine-Luzgin, M. Ito, S.V. Ketov, A.S. Trifonov, J. Jiang, C.L. Chen, K. Nakajima, Exceptionally high nanoscale wear resistance of a $Cu_{47}Zr_{45}Al_8$ metallic glass with native and artificially grown oxide, Intermetallics 93 (2018) 312–317.
[53] B. Persson, I.M. Sivebaek, V.N. Samoilov, K. Zhao, A.I. Volokitin, On the origin of Amonton's friction law, J. Phys. Condens. Matter 20 (39) (2008) 395006.
[54] F.P. Bowden, D.F. Tabor, The friction and lubrication of solids, Am. J. Phys. 2 (7) (1950) 230.
[55] Y. Zhao, Y. Wu, L. Wang, M. Zhang, X. Chen, Bio-inspired reversible underwater adhesive, Nat. Commun. 8 (2017) 2218.
[56] M. Wolloch, G. Levita, P. Restuccia, M.C. Righi, Interfacial Charge Density and Its Connection to Adhesion and Frictional Forces, Phys. Rev. Lett. 121 (2018) 026804.
[57] Z. Liu, S. Zheng, Z. Lu, J. Pu, G. Zhang, Adhesive transfer at copper/diamond interface and adhesion reduction mechanism with fluorine passivation: a first-principles study, Carbon 127 (2017) 548–556.
[58] H. Zhang, Y. Qi, J. Li, J. Wang, X. Wang, Effect of Zr content on mechanical properties of Diamond/Cu-Zr composites produced by gas pressure infiltration, J. Mater. Eng. Perform. 27 (2) (2018) 714–720.
[59] S. Lafaye, C. Gauthier, R. Schirrer, The ploughing friction: analytical model with elastic recovery for a conical tip with a blunted spherical extremity, Tribol. Lett. 21 (2) (2006) 95–99.
[60] Y.X. Ye, C.Z. Liu, H. Wang, T.G. Nieh, Friction and wear behavior of a single-phase equiatomic TiZrHfNb high-entropy alloy studied using a nanoscratch technique, Acta Mater 147 (2018) 78–89.